Design optimization of the UFSD inter-pad region

F. Siviero[a,*], R. Arcidiacono[a,b], G. Borghi[c], M. Boscardin[d], N. Cartiglia[a], M. Costa[a,e], G-F. Dalla Betta[f], M. Ferrero[a], F. Ficorella[d], M. Mandurrino[a], L. Markovic[g], L. Pancheri[f], G. Paternoster[d], V. Sola[a,e], M. Tornago[a,e]

[a] *INFN, Torino, Italy*
[b] *Università del Piemonte Orientale, Novara, Italy*
[c] *Campus Leonardo, Politecnico di Milano, Milan, Italy*
[d] *Fondazione Bruno Kessler, Trento, Italy*
[e] *Università degli Studi di Torino, Torino, Italy*
[f] *Università degli Studi di Trento, Trento, Italy*
[g] *University of Belgrade, Belgrade, Serbia*

Abstract

This paper reports on a measurement campaign to characterize the inter-pad region of Ultra-Fast Silicon Detectors (UFSDs) manufactured by Fondazione Bruno Kessler. The devices under test are either pixel or strip arrays, featuring a large number of different inter-pad layouts; both pre-irradiation and irradiated sensors have been measured. The aim of the study is to link the design parameters of the inter-pad region to the operation of the sensors, providing insights into the design of UFSD arrays with narrow inter-pad gaps. We concluded that, in the UFSD design, the doping level and the area of the p-stop should be kept low, in order to avoid the early breakdown of the device and the micro-discharges effect; UFSDs with such characteristics proved also rather insensitive to floating pads and irradiation. Thanks to these findings, it was possible to design a UFSD array that yields the expected performance with an inter-pad width as small as 25 μm, significantly improving its fill factor with respect to standard designs. Two innovative experimental techniques are presented in this work: the first one is based on a TCT setup, the second makes use of an ultra-low light CCD camera.

---

[*] Corresponding author
Email address: `federico.siviero@to.infn.it` (F. Siviero)

Keywords: UFSD, LGAD, Transient Current Technique

---

1. Introduction

Ultra-Fast Silicon Detectors (UFSDs) [1] are well-established timing detectors based on the Low-Gain Avalanche Diode (LGAD) technology [2]. UFSDs have been chosen to instrument the timing layers of the ATLAS and CMS detectors [3, 4], and are envisioned for future 4D-trackers [5, 6], namely detectors able to concurrently measure the position and time of passage of ionizing particles with ~ 10 μm and ~ 10 ps resolution, respectively. In UFSD pixel arrays, signal multiplication happens only inside the pixel, while the area in between pixels, called inter-pad or no-gain region, does not provide signal multiplication. An important line of research in the evolution of the UFSD design aims at maximizing the fill factor, i.e., the ratio between a sensor active and total areas [7, 8, 9, 10]. This paper reports an in-depth study of inter-pad designs using sensors of the UFSD3 and UFSD3.1 productions manufactured by Fondazione Bruno Kessler (FBK, Italy).

2. The FBK UFSD3 and UFSD3.1 productions

2.1. UFSD3

The third UFSD production by FBK consists of twenty 6-inch wafers (active thickness 55 μm) with five splits of gain dose and a variety of different geometries (strip arrays, 2x2 and 5x5 pixel matrices, single pads). The wafers were produced using the stepper technology instead of the mask-aligner technique previously used. This choice was made considering the better precision and higher yield offered by the stepper process.

In UFSD3, four different inter-pad designs have been implemented: *Aggressive*, *Intermediate*, *Safe*, and *Super-Safe*, with a nominal distance between gain layers of ~ 10 μm, ~ 20 μm, ~ 30 μm, and ~ 40 μm, respectively; as a reference, the inter-pad width of the previous production, UFSD2, is 70 μm. Table 1 lists these variations.

Table 1: Inter-pad design in the UFSD3 production

Name	distance [μm]
Aggressive	$\sim 10\ \ \mu$m
Intermediate	$\sim 20\ \ \mu$m
Safe	$\sim 30\ \ \mu$m
Super-Safe	$\sim 40\ \ \mu$m
Reference - UFSD2	$\sim 70\ \ \mu$m

2.2. UFSD3.1

The UFSD3.1 production was developed to study the interplay between the p-stop [1] doping levels and different layouts of the inter-pad area. It consists of seven 6-inch epitaxial wafers with an active thickness of 55 μm. All wafers have the same gain layer dose while they differ for the p-stop doping (Table 2), with doping 1 (in arbitrary unit) being the value used in UFSD2 and UFSD3. Since the goal is the comparative study of the inter-pad design, it was decided to have only one sensor layout consisting of a 2 × 2 pad matrix, with a pad size of 1.3x1.3 mm^2. UFSD3.1, as UFSD3, has been produced using the stepper lithographic technology.

The variations of the UFSD3.1 layout focused on two aspects:

1. The layout of the inter-pad region.
2. The shape of the regions where p-stops cross each other.

Figure 1 graphically describes the five designs under study:

1. Grid: p-stops form a grid around the pads
2. Full: a p-stop grid with full disks of p-doping where p-stops cross each other.

---

[1] A p-stop is a p^+-doped structure implanted in the inter-pad region to isolate two adjacent pads.

3. Empty: a p-stop grid with empty disks of p-doping where p-stops cross each other.
4. 2 p-stops: each pixel has its own p-stop.
5. Grid guard-ring: the guard-ring forms a grid, isolating each pixel. Each pixel has its own p-stop .

These five designs have been implemented with different inter-pad widths and sizes of the regions A and B, for a total of 11 different inter-pad structures, listed in Table 3.

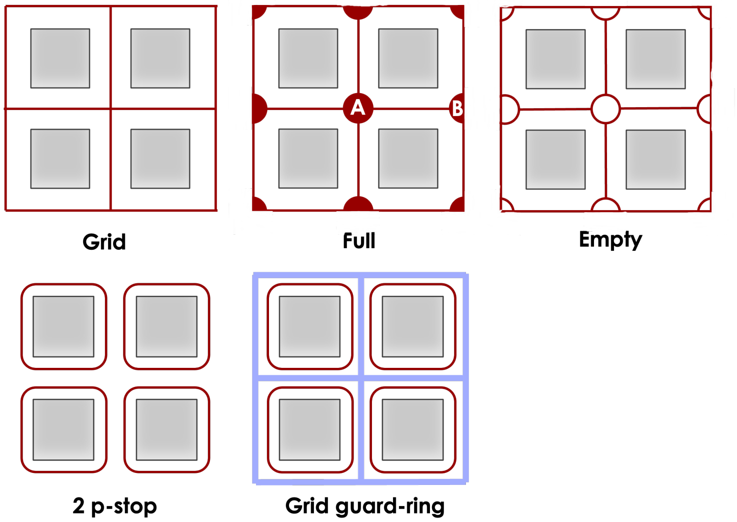

Figure 1: Sketch (not to scale) of the structures present in the inter-pad region of the UFSD3.1 design. The p-stops are shown in maroon, and the guard-ring is in blue. The areas where two p-stops cross each other (A and B in the picture) are particularly critical as they might lead to premature breakdown.

In the *grid* design, the p-stops cross each other at a 90 degrees angle, whereas in the *full* and *empty* designs, different radii of curvature are used, with large curvature radii resulting in large areas and smooth corners and small radii yielding small areas and sharper corners.

Table 2: Wafers of the UFSD3.1 production

Wafer number	p-stop doping [a.u.]
W12	0.02
W13	0.05
W14	0.1
W16	0.15
W17	0.2
W18	1

Table 3: Inter-pad design of the UFSD3.1 arrays.

Type	Nominal inter-pad width [μm]	*Region A/B* design	*Region A* area [a.u.]	*Region B* area [a.u.]
1	16	Grid	A	2B
2	20.5	Full	100A	10B
3	20.5	Full	10A	B
4	23.5	Grid	2A	2B
5	25	Full	20A	2B
6	27.5	Full	10A	B
7	27.5	Full	20A	2B
8	27.5	Grid	2A	2B
9	38	2 p-stops		
10	49	Grid guard-ring		
11	25	Empty	100A	10B

3. Experimental Techniques

Two experimental techniques have been employed in this work: the Transient Current Technique (TCT), and CCD thermal camera imaging.

3.1. *The TCT Setup*

The TCT technique exploits the motion of non-equilibrium $e-h$ pairs created by a laser entering the Device Under Test (DUT). The free charge carriers drift towards the electrodes, inducing a current signal which is a function of time. The analysis of the evolution in time of such current signal is the basis of the TCT technique, providing a wide number of detailed information about the DUT. For this analysis, the TCT set-up produced by Particulars [11, 12] was used.

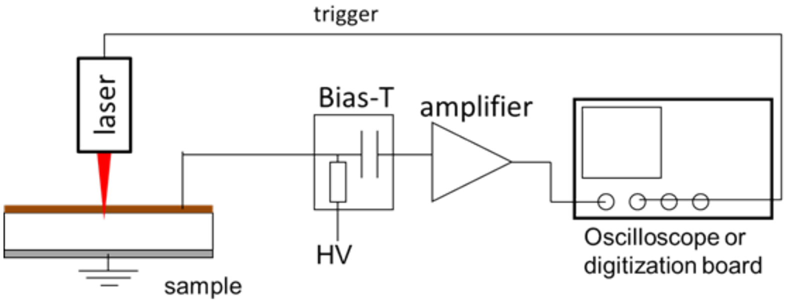

Figure 2: Princple of operation of the Transient Current Technique setup.

The basic scheme of a TCT system is shown in fig. 2: the laser lights the sensor, producing a signal that is amplified by an external trans-impedance amplifier (a 40 dB Cividec amplifier with 2 GHz bandwidth) and then fed to a fast oscilloscope (a Teledyne-Lecroy HDO9404 oscilloscope with a 20 GS/s sampling rate), where it is recorded for the offline analysis.

An important feature of the Particulars system is the possibility of mounting the DUT on a translator x-y stage (Standa 8MTF-102LS05/8MT175-100), which can be moved with sub-micron precision over a range of tens of centimeters; in this way, the laser shot position can be accurately chosen, and the whole surface of the DUT can be mapped.

The laser usually employed in the UFSD characterization is infrared with a wavelength $\lambda = 1060$ nm: its absorption depth in silicon is about 1 mm [13], so it manages to fully cross the DUT, uniformly creating charges along its path

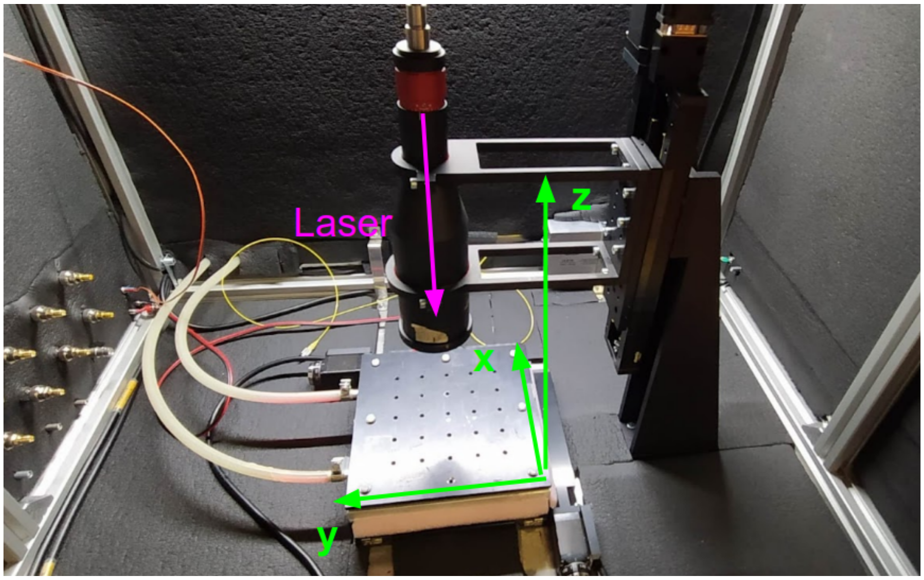

Figure 3: TCT setup in the Torino Laboratory for Innovative Silicon Detectors.

and, thus, well simulating the passage of a MIP.

The lasers used in this work, produced by Particulars, are single-mode pulsed lasers with a core diameter of $\sim 6\ \ \mu$m. The laser intensity can be varied depending on the measurement: it can be set to a level corresponding to a signal lower than that generated by a MIP, up to many hundreds of MIPs.

The lasers used in this work have frequencies in the range 50 Hz - 1 MHz and their pulse durations range from $\sim$ 50 ps to 4 ns, with symmetrical pulses.

3.2. The CCD thermal camera

A CCD thermal camera is able to perform ultra-low light imaging and it exploits photon emission to identify the location where the density of current is high.

For this work, the EM-CCD camera Hamamatsu ORCA2 C11090-22B was used [14]. It consists of a 1024×1024 pixel matrix providing 1M pixel resolution and high quantum efficiency from near-IR to UV, and it is particularly suitable for applications requiring long exposure times and low noise.

In this work, the camera is employed to take pictures of the UFSD inter-pad region. For such purpose, the camera is mounted on top of the microscope of a probe station using a specific ocular, as shown in 4; this allows examining the inter-pad region in detail.

An external module driver and dedicated software control the camera. When the camera is turned on and positioned on the ocular, it can display the field of view and take pictures. Different exposure times can be chosen, and the camera can be run both in *normal* mode (a standard CCD camera) and *gain* mode, in which the light input is multiplied by a specific gain factor that can be chosen by the user. The latter mode is useful when seeking to detect very faint light sources. The acquired picture can be either displayed in *black* & *white* or in 2-/3- colors mode. The light wavelength range in which the camera operates changes dynamically by default, but the user can also set a fixed range.

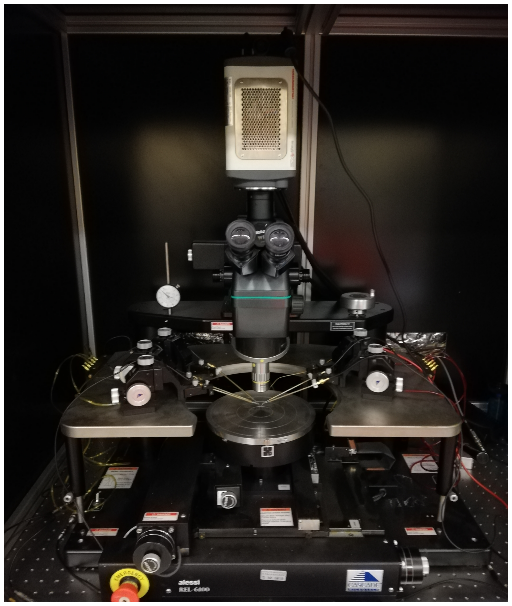

Figure 4: The ORCA2 camera mounted on the probe station of the Torino Laboratory of Innovative Silicon Sensors.

During the measurements presented in this work, performed at room temperature, the DUT is placed on the probe station metal chuck, which provides the bias voltage on the backside, while the guard-ring and the pads on the front side are contacted with needles and grounded. Then the camera is positioned on the ocular, and the microscope is manually focused, with a magnification such that all the regions of interest can be viewed.

4. Inter-pad widths of the UFSD3 and UFSD3.1: nominal vs measured

The inter-pad width of the sensors presented in this work has been measured in the laboratory, using the TCT setup. The sensors tested have a small region without metal traces (optical window) from one pad to the neighboring one, specifically designed for this measurement.

The measurement is made by performing a TCT scan between two adjacent pads and acquiring their collected charges as a function of the laser position. For each sensor to be evaluated, the scan is performed a hundred times. The uncertainty on the measured width is about 2 μm.

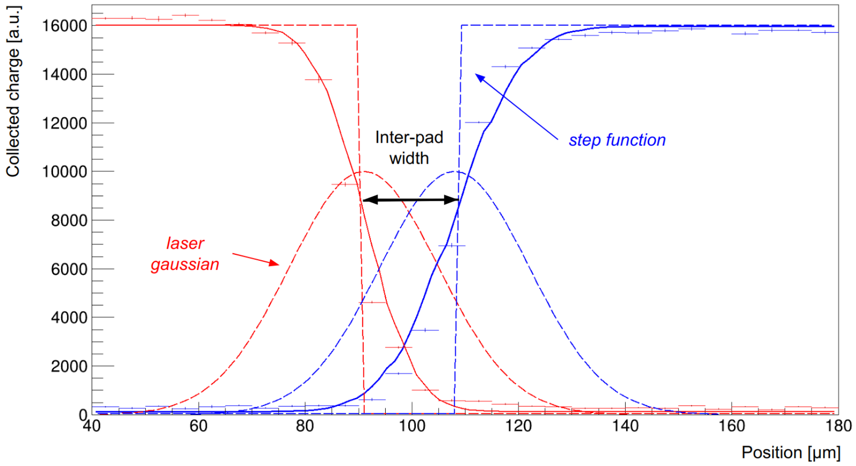

Figure 5: Collected charge as a function of position of two neighboring pads. The step function and the gaussian profile result in a sigmoidal function which is used for the inter-pad width measurement.

The expected charge profile from the acquisition consists of two sigmoidal functions (figure 5), one for each read-out pad. The sigmoid is obtained by the convolution of a step function (describing the transition between gain and no gain regions) with a gaussian function, which accounts for the laser beam spot size. The point at which the sigmoid reaches 50% of its height corresponds to the intercept with the step function used in the convolution: hence, the width of the no-gain region is given by the distance between the 50% points of the charge profiles of the two pads.

Table 4 presents the measured and nominal inter-pad widths of the sensors tested in this work. A detailed description of the inter-pad width measurement can be found in [15, 16].

Table 4: Inter-pad widths measured with the TCT setup. The uncertainty on the measured widths is ± 2 μm.

Production	design	measured inter-pad [μm]	nominal inter-pad [μm]	Thermal load
UFSD2		67	70	Low
UFSD3	*Aggressive*	16.5	11	Low
UFSD3	*Medium*	16.5	20.5	Low
UFSD3	*Medium*	31	20.5	High
UFSD3	*Safe*	30.5	31	Low
UFSD3	*Super-Safe*	38	41	Low
UFSD3.1	Type 1	32	16	High
UFSD3.1	Type 10	62	49	High
UFSD3.1	Type 11	36	20.5	High

As reported in [17], the measured inter-pad distance is always larger than the nominal one due to the bending of the electric field lines caused by the presence of the JTE structures around the pixel periphery. It is also interesting to note that sensors produced with a higher thermal load have a wider inter-pad distance.

5. The inter-pad design of the FBK UFSD3 production

The UFSD3 production aimed at exploring the stability of designs with nominal inter-pad widths in the range 11 - 49 μm, considerably reducing the values reached in the UFSD2 production ($\sim$ 70 μm).

The first step of the UFSD3 characterization was to measure the $I(V)$ characteristic of UFSD arrays with different designs, reported in Figure 6. *Super-safe* sensors, namely sensors with the largest inter-pad width, have the typical $I(V)$ curve of a sensor with gain: it follows an exponential trend till breakdown, in this case above 300 V.

Since all measured sensors have the same gain layer doping, the breakdown voltage ($V_{BD-Gain}$) due to gain is common to all. However, the *Safe*, *Medium* and *Aggressive* designs suffer from premature (or early) breakdown, with an abrupt, not exponential, $I(V)$ characteristic. In particular, Figure 6 shows that the narrower the inter-pad width, the earlier V_{BD} . The abrupt $I(V)$ curves indicate that the breakdown is not caused by an avalanche in the gain region.

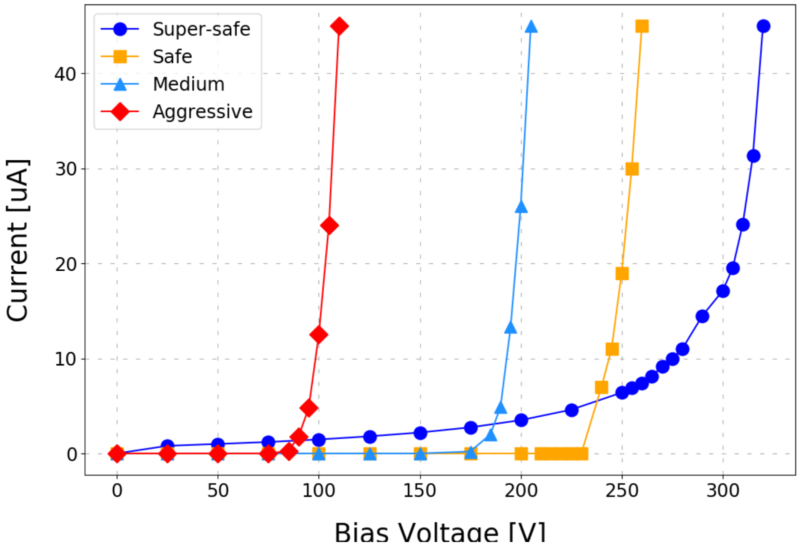

Figure 6: $I(V)$ curves of UFSD3 sensors with different inter-pad widths

Since the only difference among tested sensors is the inter-pad design, the early breakdown likely originates there. The steps taken to understand the origin of the early breakdown are explained in the following part of this section. The samples used for the study are:

- A strip sensor with *Super-safe* inter-pad design (600 μm pitch, 1 cm length)
- A 2×2 pad matrix with *Safe* inter-pad design (1×3 mm^2 pads)
- A 2×2 pad matrix with *Medium* inter-pad design (1×3 mm^2 pads)
- A strip sensor with *Medium* inter-pad design (300 μm pitch, 1 cm length)
- A 2×2 pad matrix with *Aggressive* inter-pad design (1×3 mm^2 pads)

The working hypothesis has been that the early breakdown happens somewhere in the inter-gap region, and in this spot, a high electric field should be present. This high electric field generates local multiplication of the charge carriers, yielding localized gain and photon emission.

All DUTs are covered with a metal layer over the gain region, with the exception of the optical windows used for the inter-pad measurement. Therefore, only the no-gain and optical window areas could be scanned with the TCT setup. The measurements have been performed at room temperature, with the sensor bonded to a custom read-out board. Each read-out channel is connected to a 40-dB external broadband amplifier, whose output is then connected to a fast oscilloscope.

The DUTs are firstly scanned at a voltage well below breakdown to record the collected charge and produce an x-y map that clearly defines the DUT and, in particular, the inter-pad region. As an example, Figure 7 on the left shows the layout of the sensor, while on the right the TCT collected charge (sensor with *Safe* design). The z-axis (color-coded) reports the sum of the charges collected by all four pads. The gain regions covered by the metal have a collected charge close to zero (in blue).

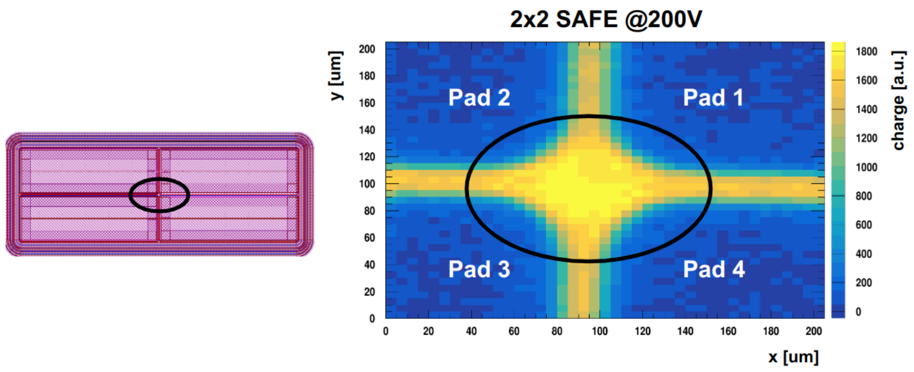

Figure 7: Left: sensor layout, right: 2D-map of the charge collected in a sensor with *Safe* design.

The three plots of Figure 8 show, for Pad 1, the evolution of the collected charge as a function of the bias voltage. The charge is constant across the inter-pad region at 200 V; it increases significantly at 250 V, and at 260 V, the breakdown begins. Figure 9 shows the x-projection of these 2D-maps at y=100 μm where the current increase with bias at x = 120 μm signals the onset of the breakdown.

Figure 10 shows a similar result for the strip sensor with *Medium* design: the charge collected around the strip corner (y = 150 μm) is constant at 200 V, then increases approaching breakdown.

The *Super-safe* sensor, instead, does not show any increase in collected charge in the inter-pad region when brought into breakdown, as shown in 11: this is the only design able to reach the expected breakdown voltage $V_{BD-Gain}$.

Hence, sensors suffering from premature breakdown show signs of charge multiplication occurring in the inter-pad region, whereas the *Super-safe* devices have a constant collected charge in the inter-pad up to breakdown. The charge multiplication in the inter-pad region is caused by the onset of a strong electric field, underlying a weakness in the design. The effect of such a field appears suddenly, as proven by the trend of the $I(V)$ curves in those devices.

The high electric field occurring in the inter-pad region can be explained as due to the *pn* junction between the *p*-stop and the *inversion layer* underneath

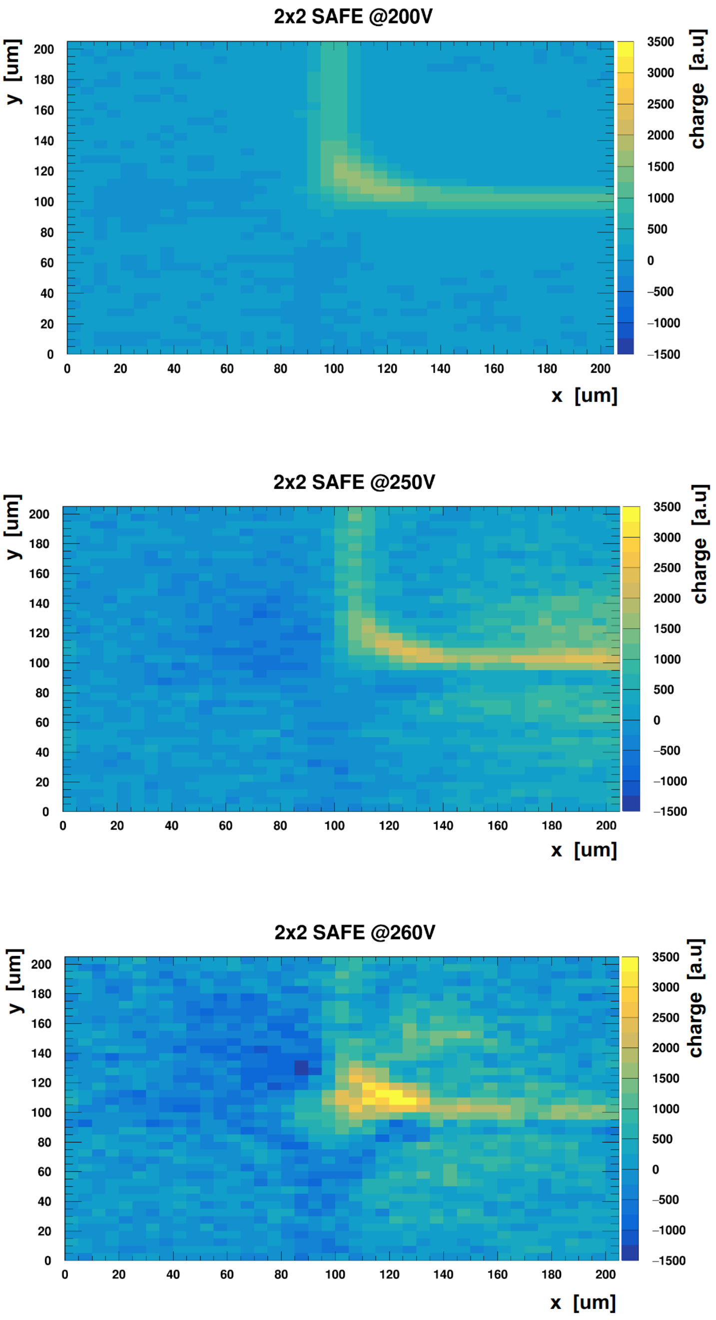

Figure 8: TCT 2D-map of the charge collected by Pad 1 at three different bias voltages: 200 V, 250 V, and 260 V.

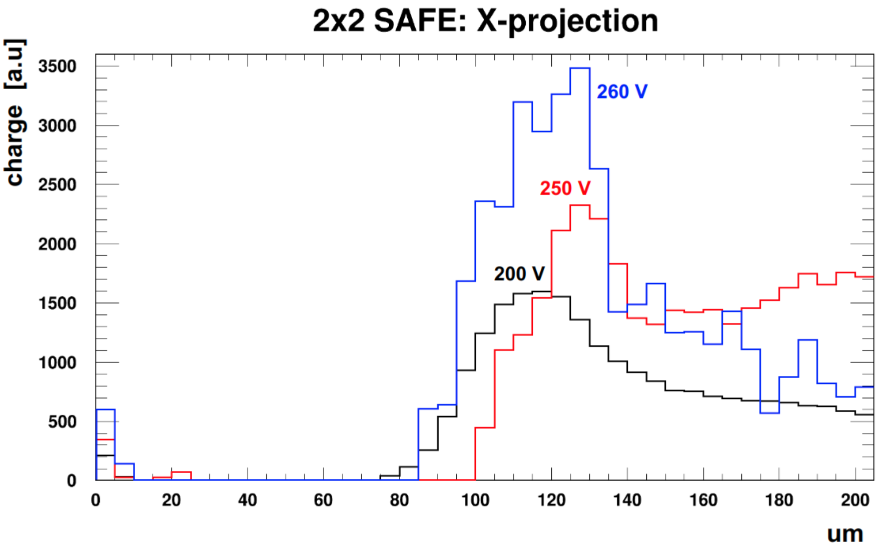

Figure 9: X-projections of the 2D-maps shown in figure 8 at y=100 μm. The current increase with bias at x = 120 μm signals the onset of the breakdown.

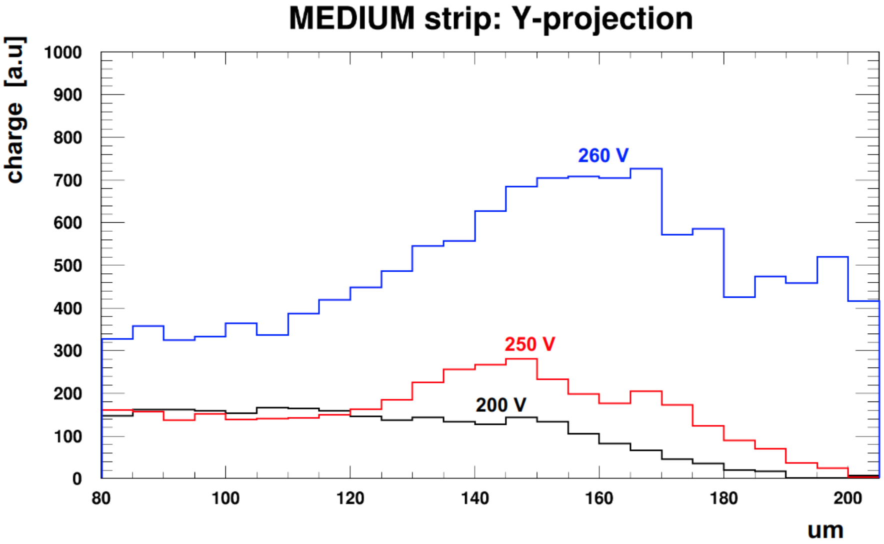

Figure 10: Charge collected in the inter-pad region by a strip sensor with Medium design for three different voltages.

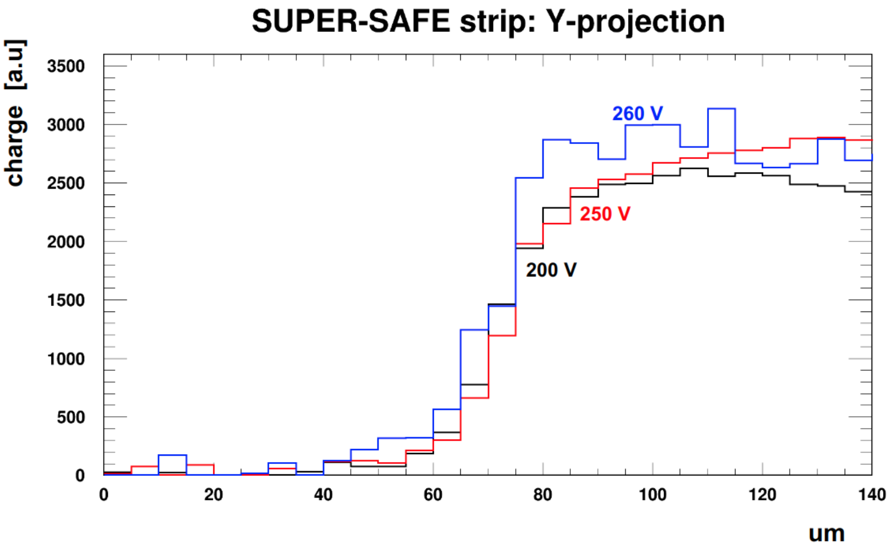

Figure 11: Charge collected in the inter-pad region by a strip sensor with Super-safe design for three different voltages.

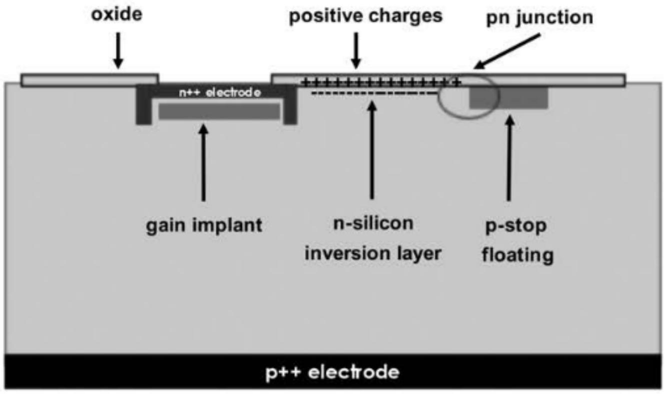

Figure 12: Schematic representation of the inversion layer establishing in the inter-pad region.

the oxide due to the positive charges present at the Si-SiO_2 interface. A sketch is shown in Figure 12. The value of the p-stop doping determines how abrupt is the pn junction and, consequently, how high the electric field is [18]. It follows that high p-stop doping leads to higher fields, therefore, weakening the sensor design.

The intensity of the electric field between the pixel and the p-stop is also affected by their relative distance and the sensor thickness. The p-stop is electrically floating, and it positions itself at a potential between the backplane bias voltage and the ground level of the pixel. In thin sensors, the p-stop will float to values closer to the backplane voltage, yielding a higher electric field in the region pixel-p-stop . In sensors with narrow inter-pad regions, this effect is particularly important and can lead to an early breakdown.

To confirm the results obtained with the TCT analysis, complementary studies have been conducted using a CCD thermal camera. The area of the inter-pad region scanned with the TCT has been captured with the ORCA2 camera at different bias voltages. Figures 13 and 14 show pictures of a 2×2 array with *Safe* design, and of the strip device with *Super-safe* design, taken before and after breakdown.

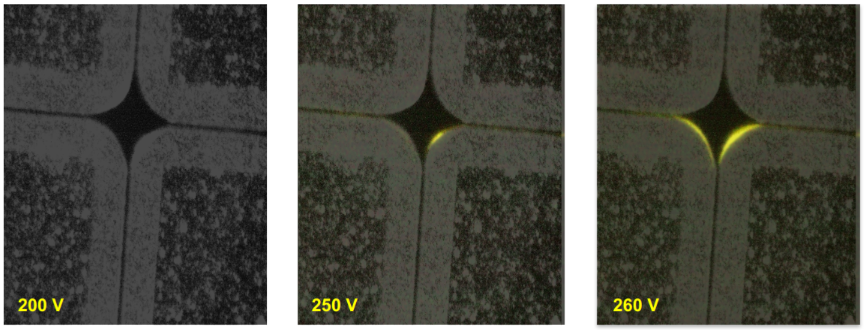

Figure 13: Pictures of the inter-pad region of the 2×2 device with *Safe* design at three different voltages. The brighter area indicates the presence of high current density.

The *hot spots* (yellow regions) that can be seen in Figure 13 are regions that emit visible photons due to the high current densities flowing through. Such high densities are tied to the gain avalanche occurring while the sensor is going into breakdown, as previously shown with the TCT scans. *Hot spots* are particularly visible in correspondence to the corners, where the electric field is higher. Similar pictures have been obtained from the devices with *Aggressive* and *Medium* designs. As expected, the *Super-safe* device does not show any

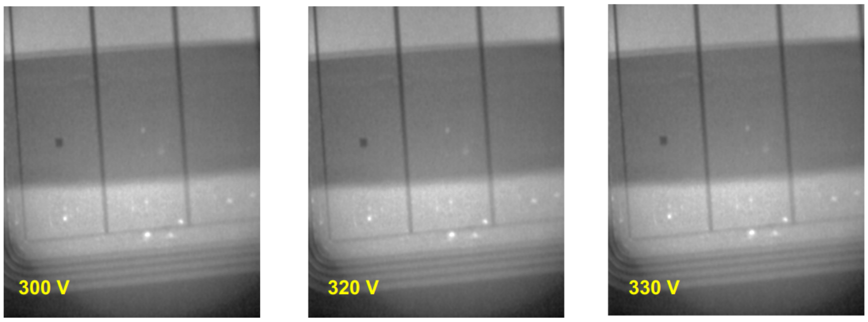

Figure 14: Pictures of the inter-pad region of the strip device with Super-safe design at three different voltages

signs of *hot spots*, see Figure 14.

5.1. Micro-discharges in UFSD3 sensors

A second undesired effect has been observed on sensors of the UFSD3 production: the appearance of large current spikes much before the breakdown voltage, which prevents proper operation of the sensor as the dark count rate increases significantly. Such large spikes have amplitude comparable to that of real signals and are randomly distributed in time [16, 19, 20]. Figure 15 presents a comparison between the normal baseline activity of a UFSD and that of a device affected by micro-discharges. The micro-discharges appear on both strip and pad sensors; they do not depend on the sensor geometry or the inter-pad designs and have been observed on both new and irradiated devices.

It is worth pointing out that the increase of the baseline activity naturally happens in all UFSD devices a few volts before breakdown: it is an indication that the gain avalanche is going to start. What distinguishes the micro-discharges in UFSD3 is they appear at a voltage much lower than $V_{BD-Gain}$.

To observe the micro-discharges, the DUT has been bonded on a custom read-out board with all channels connected to an oscilloscope. The measurements are performed inside a climate chamber, at +20 °C, with dry air fluxed. The bias voltage is raised slowly in steps of 5-10 V until the breakdown occurs; meanwhile, the baseline activity is monitored on the oscilloscope.

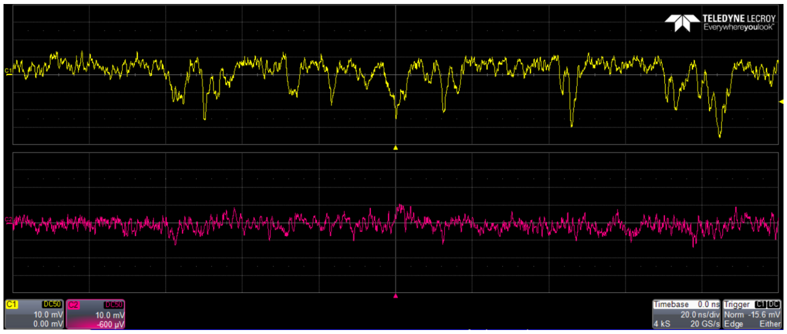

Figure 15: Comparison between a sensor with normal baseline activity (pink) and a sensor with micro-discharge (yellow). The vertical scale is 10 mV/division.

5.2. Conclusions of the measurement campaign on UFSD3

Two main issues have been identified in UFSD3:

- The sensors with *Aggressive*, *Medium* and *Safe* designs suffer from premature breakdown.
- All designs show micro-discharges much before the breakdown, which prevents the proper operation of the sensors.
- The *Super-safe design* shows micro-discharges without going into premature breakdown because the JTE and p-stop are relatively far away. Despite that, its proper operation is compromised.

The TCT scans and the measurements with the ORCA2 camera demonstrated that the issues of the UFSD3 production are tied to the strong electric fields established in the inter-pad region between the JTE and the p-stop. Such electric fields are caused by:

- Highly doped p-stops
- A short distance between the JTE and the p-stops

6. Measurement campaign on UFSD3.1 sensors

The UFSD3.1 production was designed to explore further the properties of the UFSD inter-pad region. The measurement campaign started analyzing the $I(V)$ characteristics of several devices: a summary is shown in Figures 16. Figure 16 (a) reports the $I(V)$ characteristics of sensors with the same inter-pad design (Type 2) and different p-stop dopings, while figure 16 (b) reports the $I(V)$ characteristics of sensors with the same p-stop doping and different inter-pad designs.

The breakdown voltage due to gain, $V_{BD-Gain}$, is expected to be 360-380 V for all sensors as they share the same gain layer dose: sensors going into breakdown earlier are considered to be suffering from premature breakdown.

Figure 16 (a) shows the strong influence of the p-stop doping on V_{BD} . Given that all sensors are of Type 2, the difference in V_{BD} is due solely to the p-stop doping level. For high values of p-stop doping V_{BD} decreases considerably while for low values V_{BD} reaches its limiting value $V_{BD-Gain}$. Conversely, Figure 16 (b) shows the influence of the inter-pad design on V_{BD} , as all sensors have the same p-stop doping. The combination of the two plots clearly demonstrates the interplay of doping and geometry: a given type, for example Type 2, has an early breakdown if the p-stop is too doped, while a stronger design, for example Type 4, does not have an early breakdown even with a high p-stop doping.

The ORCA2 camera detects *hot spots* much more rapidly than the TCT procedure, so it was used to test numerous devices. The measurements have been performed with the procedure described in Section 5.1. A few examples are shown in 17, 18. The remarkable feature of the ORCA2 testing campaign was that all sensors with premature breakdown show *hot spots* near the *Regions A/B* and not along the p-stop perimeter.

Figure 19, left side, shows that as the area of the region *Region A* increases, V_{BD} decreases. Sensors with less-doped p-stops, those on W13, are less sensitive to this effect. A similar result is obtained when considering V_{BD} as a function

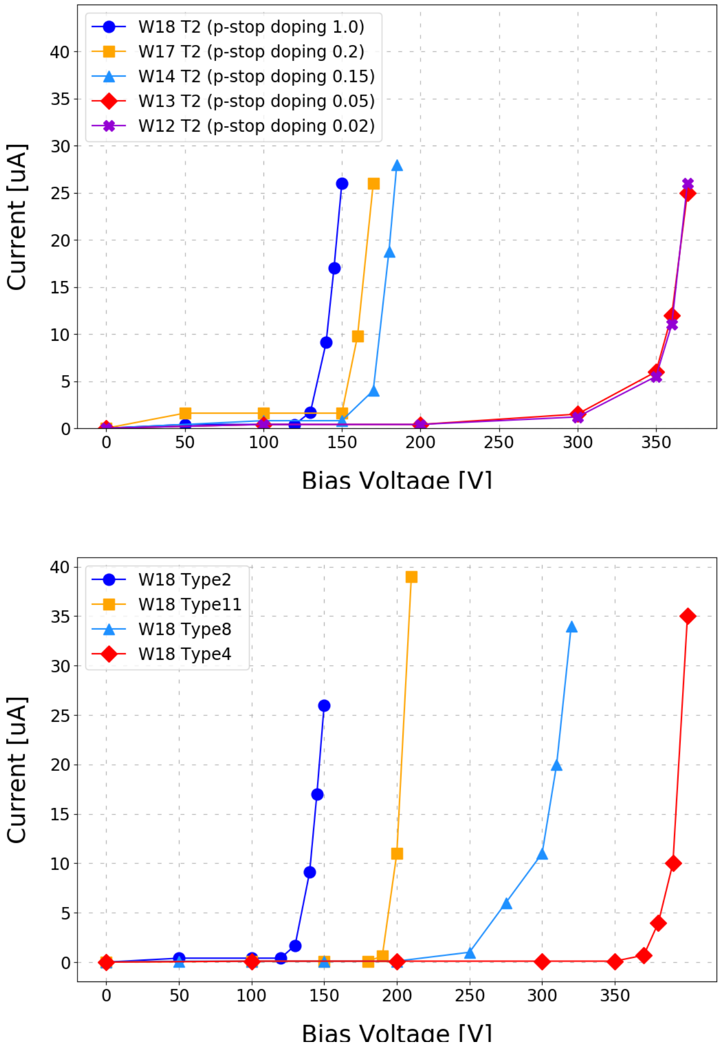

Figure 16: Top: $I(V)$ of devices with different p-stop dopings having the same inter-pad design (Type 2). Bottom: $I(V)$ of devices with different inter-pad design having the same p-stop doping.

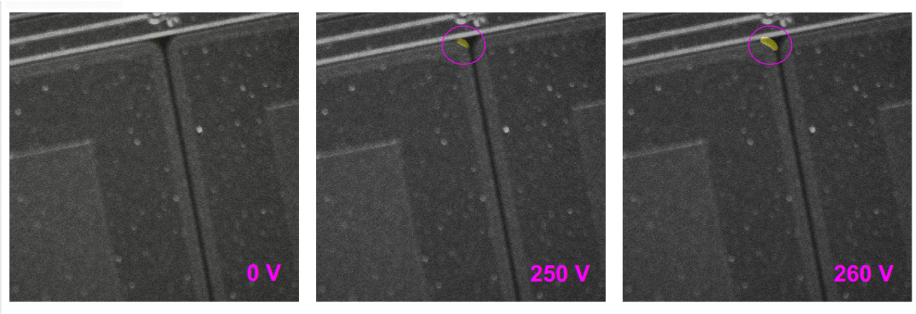

Figure 17: *Hot spots* in a Wafer18 Type 2 sensor near *Region B*

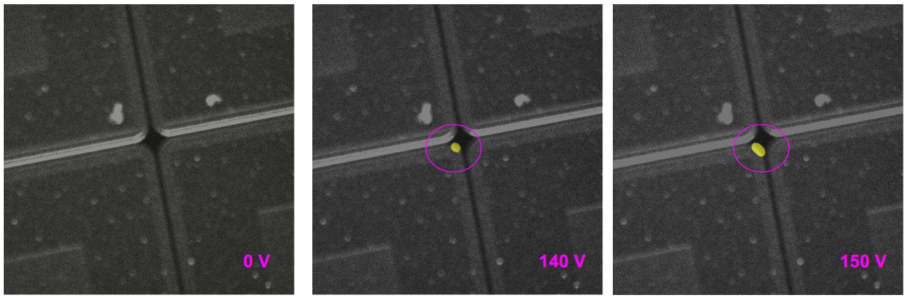

Figure 18: *Hot spots* in a Wafer14 Type 1 sensor near *Region A*

of the *Region B* area.

Figure 19, right side, instead, highlights that a less-doped p-stop allows to reach a higher V_{BD} . Types 3 and 4 have a low dependence on the p-stop doping because they have small *Region A, B* areas; Type 10, instead, is not susceptible to the p-stop doping because of its grid guard-ring design. Type 1 has small p-structures but its V_{BD} depends strongly on the p-stop doping since it features the most aggressive design. The figure also shows that sensors from the wafers with lowest p-stop dopings (W12 and W13) have a V_{BD} that reaches the limiting value of 360-380 V.

In wafers 12 and 13 the p-stop dose is such that the breakdown always happens due to internal gain, regardless of the inter-pad design. Wafer 14 shows a similar trend, with only the most aggressive designs going into an early

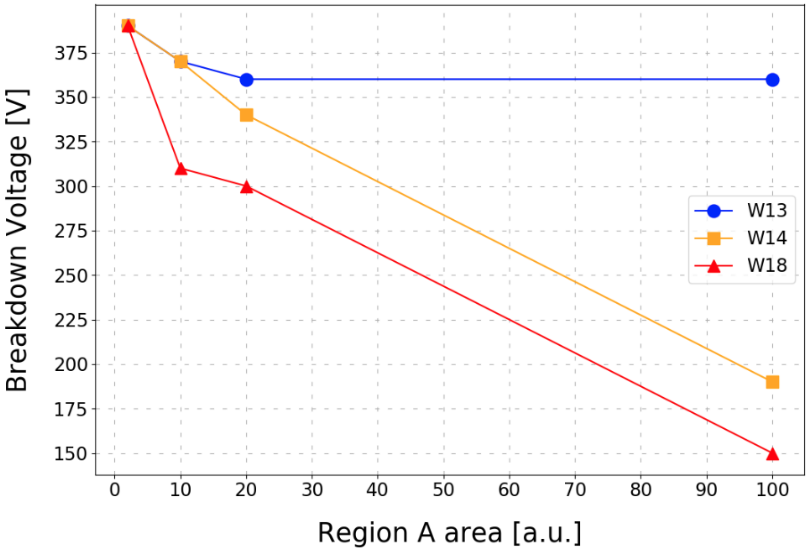

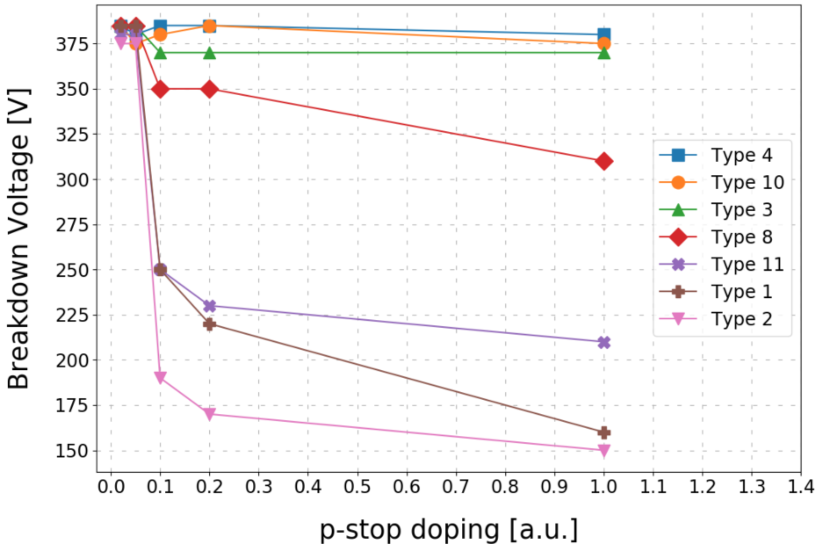

Figure 19: Top: V_{BD} as a function of *Region A* area for different Wafers (different p-stop doping). Bottom: V_{BD} as a function of p-stop doping for different sensor types.

breakdown.

The results of this measurement campaign can be summarized as follows:

- Premature breakdown occurs in the inter-pad region near the pad corners.
- Premature breakdown depends both on the p-stop doping and on the inter-pad design/width.
- Corners (*Regions A, B*) are the most critical areas.
- Large and/or too-doped p-structures lead to premature breakdown, preventing proper operation of sensors.
- The combination of low-doped p-stop and small-area *A, B regions* is the optimal choice to avoid early breakdown.
- An inter-pad width of $\sim 25\ \ \mu$m is achievable without incurring in premature breakdown (UFSD3.1 Type 4), adopting low-doped p-stops. Sensors with narrower regions (Type 1) are unstable.

6.1. The effect of floating pads on V_{BD} .

The breakdown voltage of several UFSD3.1 2×2 devices with 0, 1, and 2 floating pads has been measured for several wafers. Figure 20 left side, shows that sensors from W13 (low p-stop doping) are almost insensitive to floating pads, whereas, Figure 20 right side, most sensors from W18 (high p-stop doping) have a breakdown voltage decreasing with the number of floating pads. This study confirms the key importance of a low-doped p-stop to assure stable V_{BD} even in non-standard working conditions such as those with one or more floating pads. Type 10, due to its grid guard-ring design, is very resilient to floating pads, regardless of the p-stop doping.

6.2. Micro-discharges in UFSD3.1

UFSD3.1 Wafers 13 and 14 have been tested for the micro-discharges effect, following the same procedure described for the UFSD3 production, see Section 5.1. The results are reported in Tables 5 and 6.

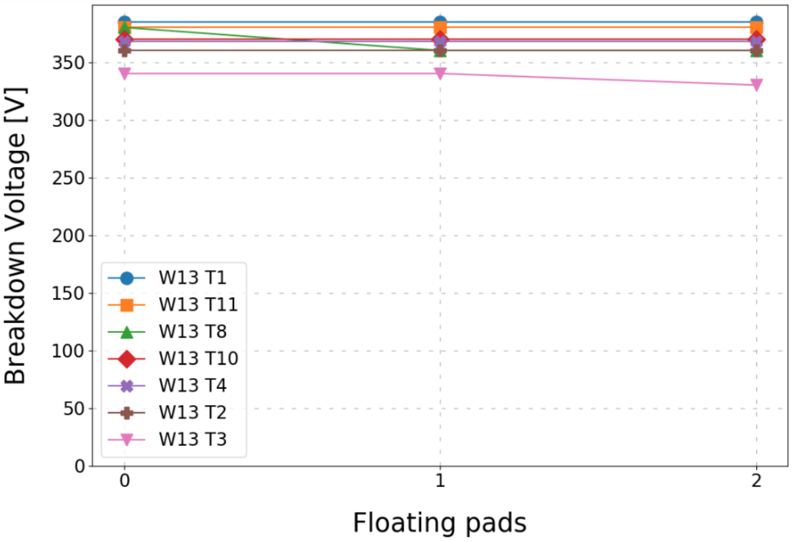

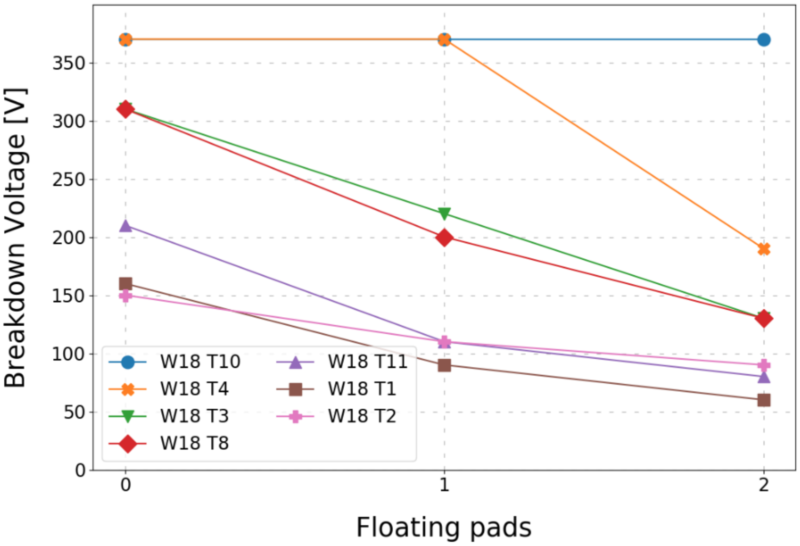

Figure 20: Top: V_{BD} as a function of the number of floating pads for different sensor designs from Wafer 13. Types 4 and 10 have the same V_{BD} (370 V), but the curves have been slightly shifted for illustration purposes. Bottom: V_{BD} as a function of the number of floating pads for different sensor designs from Wafer 18.

	0 pad floating			1 pad floating		
Type	V_{BD}	Discharge	$V_{Discharge}$	V_{BD}	Discharge	$V_{Discharge}$
Type 1	385	NO		350	NO	
Type 8	380	NO		380	NO	
Type 9	365	NO		355	NO	
Type 10	370	NO		335	NO	
Type 11	380	NO		335	NO	

Table 5: Results on the micro-discharges effect on UFSD3.1 W13.

	0 pad floating			1 pad floating		
Type	V_{BD}	Discharge	$V_{Discharge}$	V_{BD}	Discharge	$V_{Discharge}$
Type 1	260	YES	245	170	YES	145
Type 8	350	NO		350	NO	
Type 9	370	NO		310	NO	
Type 10	380	NO		380	NO	
Type 11	250	NO		185	NO	

Table 6: Results on the micro-discharges effect on UFSD3.1 W14.

Wafer 13 does not show any signs of discharges, even with one pad floating; whereas wafer 14 has some, occurring 15-25 V before the breakdown, but only in the Type 1 design, which is the most aggressive. Micro-discharges are, therefore, not an issue for UFSD3.1 wafers with low *p*-stop doping since they are present only in the most aggressive design of W14, and only very close to breakdown, not affecting the device operation.

Radiation damage has two main effects that can influence the presence of micro-discharges: (i) the sensor is operated at higher bias voltage; (ii) the *acceptor removal* mechanism [21] decreases the doping of the *p*-stop structures. The two effects act in opposite directions: (i) leads to an increase in the electric field, whereas (ii) lowers it. Table 7 reports the results obtained on wafer 14, irradiated at $\phi = 4 \cdot 10^{14}$ $\mathrm{n_{eq}/cm^2}$ and $\phi = 8 \cdot 10^{14}$ $\mathrm{n_{eq}/cm^2}$. The sensors have been irradiated, without bias, with neutrons at the JSI TRIGA research reactor in Ljubljana [22]. Types 1 and 11 show micro-discharges at $\phi = 4 \cdot 10^{14}$ $\mathrm{n_{eq}/cm^2}$, whereas only Type 1 features this effect at $\phi = 8 \cdot 10^{14}$ $\mathrm{n_{eq}/cm^2}$. Similar results are obtained in the "1 floating pad" configuration: only types 1 and 11 show signs of micro-discharges. Interestingly, at $\phi = 1.5 \cdot 10^{15}$ $\mathrm{n_{eq}/cm^2}$, all types break down above 600 V, and none has micro-discharges before V_{BD} .

	$\phi = 4 \cdot 10^{14}$ $\mathrm{n_{eq}/cm^2}$			$\phi = 8 \cdot 10^{14}$ $\mathrm{n_{eq}/cm^2}$		
Type	V_{BD}	Discharge	$V_{Discharge}$	V_{BD}	Discharge	$V_{Discharge}$
Type 1	390	YES	270	440	YES	390
Type 8	470	NO		510	NO	
Type 9	470	NO		540	NO	
Type 10	500	NO		590	NO	
Type 11	430	YES	300	530	NO	

Table 7: Results on the micro-discharges effect on UFSD3.1 W14 irradiated.

Radiation damage, therefore, does not trigger the presence of micro-discharges, even if the sensors are operated at a much higher bias voltage.

6.3. W14 inter-pad resistance

The main task of the *p*-stop implant is to assure pixel isolation by interrupting the charge inversion layer, as shown in Figure 12. This can only happen if the *p*-stop doping level is high enough. It is, therefore, mandatory to check that inter-pad resistance remains high at all *p*-stop dose levels considered, before and after irradiation.

The chosen figure of merit that quantifies the pad isolation is the inter-pad resistance, namely the resistance of a pad to ground when all the other pads and the guard-ring are connected to ground. The measurements have been performed on 2×2 pad arrays of types 8, 9, and 10, at +20 °C. Three pads and the guard-ring are grounded, while a voltage sweep between -10 V and +10 V is performed on the pad under test, as shown in Figure 21. The measured current

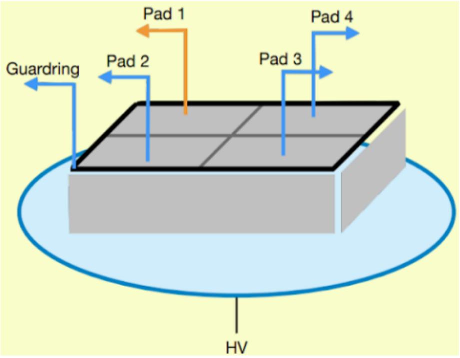

Figure 21: Sketch of the setup used to measure the inter-pad resistance.

is plotted as a function of the bias voltage applied to the pad: the slope of the curve provides the inter-pad resistance. That is actually a lower limit, since the measurement does not account for the bulk current, which should be subtracted from the measured current, thus yielding a larger inter-pad resistance.

The measurement is performed on a pre-irradiation sensor and repeated on devices irradiated at $\phi = 4 \cdot 10^{14}$ $\mathrm{n_{eq}/cm^2}$, $\phi = 8 \cdot 10^{14}$ $\mathrm{n_{eq}/cm^2}$, $\phi = 1.5 \cdot 10^{15}$ $\mathrm{n_{eq}/cm^2}$, and $\phi = 3 \cdot 10^{15}$ $\mathrm{n_{eq}/cm^2}$.

The results are shown in Figure 22: the resistance lowers with increasing exposure, but it remains high, about 10 GΩ, even at the highest fluence, proving that the pad is well isolated. As a comparison, the UFSDs that will instrument the CMS Endcap Timing layer must have an inter-pad resistance higher than 0.1 GΩ up to a radiation fluence of $1.5 \cdot 10^{15}$ $\mathrm{n_{eq}/cm^2}$ [23].

7. Conclusions

The development of LGADs array with high fill factor requires the study of the property of the inter-pad region. Two FBK productions, UFSD3 and UFSD3.1 have been dedicated to this analysis.

The main conclusion of the studies presented in the paper is that a high *p*-stop doping leads to early breakdown and micro-discharges. When using a

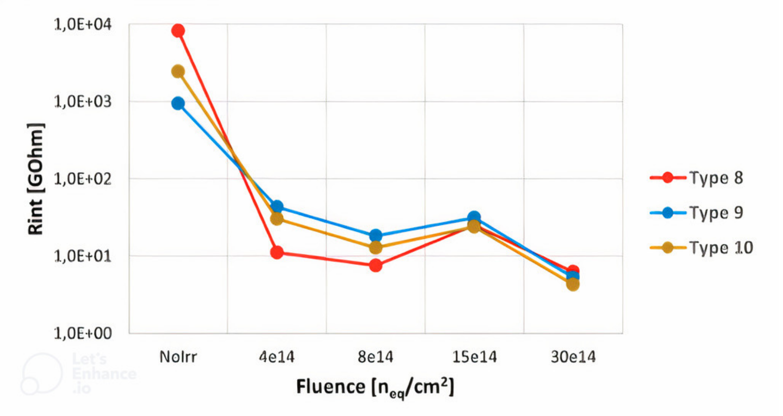

Figure 22: Inter-pad resistance of UFSD3.1 W14 as a function of fluence.

p-stop grid and low *p*-stop doping, inter-pad distances as small as 25 μm are achievable.

UFSDs with a low-doped *p*-stop, and small-area structures in the inter-pad region have also been proven to be rather insensitive to floating pads and irradiation up to a fluence of $1.5 \cdot 10^{15}$ n_{eq}/cm^2. Pad isolation is not an issue either, even for highly irradiated devices.

8. Acknowledgements

Part of this work has been financed by the European Union Horizon 2020 Research and Innovation funding program, under Grant Agreement no. 654168 (AIDA-2020) and Grant Agreement no. 669529 (ERC UFSD669529), by the Italian Ministero degli Affari Esteri, by INFN Gruppo V and by the Dipartimento di Eccellenza, University of Torino (ex L. 232/2016, art. 1, cc. 314, 337). The work was supported by the United States Department of Energy, grant DE-FG02-04ER41286.

References

[1] H. F. W. Sadrozinski, et al., Ultra-fast silicon detectors (UFSD), Nucl. Inst. Meth. A 831 (2016) 18. `doi:10.1016/j.nima.2016.03.093`.

[2] G. Pellegrini, et al., Technology developments and first measurements of low gain avalanche detectors (LGAD) for high energy physics applications, Nucl. Inst. Meth. A 765 (2014) 12–16. `doi:10.1016/j.nima.2014.06.008`.

[3] CMS Collaboration, A MIP Timing Detector for the CMS Phase-2 Upgrade, CERN-LHCC-2019-003, CMS-TDR-020 (2019).

[4] ATLAS Collaboration, Technical Design Report: A High-Granularity Timing Detector for the ATLAS Phase-II Upgrade, CERN-LHCC-2020-007, ATLAS-TDR-031 (2020).

[5] ECFA Detector R&D Roadmap Process Group, The 2021 ECFA detector research and development roadmap, CERN-ESU-017 (2020). `doi:10.17181/CERN.XDPL.W2EX`.

[6] N. Cartiglia, et al.,LGAD designs for Future Particle Trackers, Nucl. Inst. Meth. A, 979 (2020) 164383. `doi:10.1016/j.nima.2020.164383`.

[7] G. Paternoster, et al.,Novel strategies for fine-segmented Low Gain Avalanche Diodes, Nucl. Inst. Meth. A, 987 (2021) 164840. `doi:10.1016/j.nima.2020.164840`.

[8] R. Arcidiacono, et al.,State-of-the-art and evolution of UFSD sensors design at FBK, Nucl. Inst. Meth. A, 978 (2020) 164375. `doi:10.1016/j.nima.2020.164375`.

[9] S. Wada, et al.,Design of a Segmented LGAD Sensor for the Development of a 4-D Tracking Detector, Pos Proc. Sci., in: Proceedings of Vertex 2019: the 28th International Workshop on Vertex Detectors. `doi:10.22323/1.373.0057`.

[10] K. Nakamura and S. Kita and T. Ueda and K. Hara and H. Suzuki, First Prototype of Finely Segmented HPK AC-LGAD Detectors, JPS Conf. Proc., 34 (2021) 010016. `doi:10.7566/JPSCP.34.010016`.

[11] `http://particulars.si`.

[12] G. Kramberger,Advanced Transient Current Technique Systems, PoS Proc. Sci 373(Vertex2014) (2015) 32. `doi:10.22323/1.227.0032`.

[13] M.A. Green and M. Keevers, Optical properties of intrinsic silicon at 300 K, Progress in Photovoltaics, 3, (1995).

[14] `https://www.hamamatsu.com/eu/en/product/cameras/cmos-cameras/index.html`.

[15] P. Skomina and B. Hiti and V. Cindro and A. Howard and I. Mandić and M. Mikuž and G. Kramberger, Studies of inter-pad distance in low gain avalanche detectors, Nucl. Inst. Meth. A, (2021) 158–166. `doi.org/10.1016/j.nima.2021.166158`.

[16] F. Siviero, Innovative TCT studies on the breakdown of UFSD3 sensors by FBK, in 33rd RD50 workshop (2018). `https://indico.cern.ch/event/754063/contributions/3222653/`.

[17] M. Ferrero, et al., Ultra-fast silicon detectors : design, tests, and performances, CRC Press, 2021. `doi:10.1201/9781003131946`.

[18] M. Printz, P-stop isolation study of irradiated n-in-p type silicon strip sensors for harsh radiation environments, Nucl. Inst. Meth. A, 831 (2016) 38–43. `doi:10.1016/j.nima.2016.05.103`.

[19] Y. Unno, et al., Optimization of surface structures in n-in-p silicon sensors using TCAD simulation, Nucl. Inst. Meth. A, 636 (2011) 118–224.

[20] F. Hartmann, Evolution of Silicon Sensor Technology in Particle Physics, Springer Tracts Mod. Phys., 275 (2017) 1–372. `doi:10.1007/978-3-319-64436-3`.

[21] M. Ferrero, et al., Radiation resistant LGAD design, Nucl. Inst. Meth. A 919 (2019) 16–26. `doi:10.1016/j.nima.2018.11.121`.

[22] L. Snoj, G. Žerovnik, A. Trkov, Computational analysis of irradiation facilities at the JSI TRIGA reactor, Appl. Radiat. Isot. 70 (3) (2012) 483–488. `doi:10.1016/j.apradiso.2011.11.042`.

[23] Supply of LGAD sensors for the CMS MIP Timing Detector Endcap: 07010202M, `http://cds.cern.ch/record/2777890`.